Chapter 5
IRAS 15398–3359

5.1 Introduction

In L1527, it has been demonstrated that the kinematic structures of the infalling-rotating envelope and the outflow cavity wall are explained by the simple models (Chap. 4). Especially, the discovery of the centrifugal barrier in an infalling-rotating envelope and the chemical change across the centrifugal barrier provide us with a completely new insight in disk formation study. It is now required to confirm whether such kinematic and chemical structures are common in low-mass protostellar sources. In this chapter, a similar analysis is conducted in another WCCC source IRAS 15398−3359. While the structure of the outflow in L1527 has been analyzed based on the analysis of its envelope, the results from the clear outflow components in IRAS 15398−3359 is utilized to investigate the envelope structure.

It is still unknown when and how disks are formed in the star formation process. This is because that overwhelming emission from protostellar envelopes and outflows generally make it difficult to identify possible disks in Class 0 sources. Even absence of such a disk down to 45 au is claimed for the Class 0 protostar NGC 1333 IRAS 2A [3, 13]. Since possible disk structures in Class 0 sources are expected to be compact, high spatial-resolution and high sensitivity observations are indispensable to detect them.

IRAS 15398−3359 is a low-mass Class 0 protostar in the Lupus 1 molecular cloud ($d \sim 155$ pc [11]). A molecular outflow was detected by single-dish observations of CO emission [27, 30]. The CO ($J = 3 - 2$) observation with the James Clerk Maxwell Telescope ($\theta_{\rm HPBW} \sim 15''$) showed that the red- and blue-shifted lobes of this source were relatively overlapped with each other, and thus a pole-on geometry was suggested [30]. [12] observed H_2CO and CS lines toward this source to search for a sign of an infall motion without success. On the other hand, [9] reported the presence of an inverse P-Cygni profile of the H_2O ($1_{1,0} - 1_{0,1}$) at 557 GHz, indicating an infall

This chapter has been published in Oya et al., 2014, ApJ, 795, 152. © AAS. Reproduced with permission.

Y. Oya, *A Few Tens au Scale Physical and Chemical Structures Around Young Low-Mass Protostars*, Springer Theses, https://doi.org/10.1007/978-981-19-1708-0_5

motion of the envelope on a scale of about 10^4 au. [7] detected a ring structure in the $H^{13}CO^+$ ($J = 4 - 3$) line at a (150 − 200) au scale. They proposed that a recent accretion burst in this source enhanced the luminosity leading the H_2O evaporation, which would destruct HCO^+ in the vicinity of the protostar and cause the observed ring structure.

IRAS 15398−3359 shows peculiar chemical features. Various carbon-chain molecules, such as CCH, C_4H, and CH_3CCH are detected toward this source, which is characteristic to so-called warm carbon-chain chemistry (WCCC) [22, 24, 25]. As demonstrated in Chaps. 3 and 4, the kinematic structure of the envelope in another WCCC source, L1527, is well reproduced by the infalling-rotating envelope model. Because of the chemical resemblance of IRAS 15398−3359 to L1527, it is interesting to compare the physical structures of their envelopes. A deep insight into envelope structures of Class 0 protostellar sources is essential to explore when and how rotationally-supported disks are formed around protostars. With these motivations, several molecular lines are observed with ALMA toward IRAS 15398−3359.

5.2 Observations

ALMA observations toward IRAS 15398−3359 were carried out on December 31st, 2012 during its Cycle 0 operations. Spectral lines of CCH and H_2CO were observed with the Band 7 receiver at frequencies of (349 − 364) GHz, as listed in Table 5.1. These observations were carried out with twenty-five antennas with the baseline length ranging from 13 to 338 m. The field center of the observations was set to be $(\alpha_{2000}, \delta_{2000}) = (15^h43^m02^s.3, -34°09'07''.5)$. The system temperature was typically from 120 to 300 K. The frequency resolution of the backend correlator was tuned to be 122 kHz and bandwidth of 469 MHz, corresponding to the velocity resolution of 0.1 km s^{-1} at 366 GHz. The phase calibrations were carried out on J1517−243 for every 12 min. J1256−057 and J1924−292 were used for the bandpass calibrations. The absolute flux density scale was derived from Mars and Titan. The data calibration was performed in the antenna-based manner where typical uncertainties are expected to be less than 10%. The primary beam (half-power beam width) is 17″. CLEAN algorithm was employed to obtain the continuum and line images. The continuum image was obtained by averaging line-free channels. After subtracting the continuum emission directly from the visibilities, the line images were obtained. The total on-source time was 27 minutes and 21 minutes for the H_2CO lines and the CCH lines, respectively. The synthesized-beam size is $0''.57 \times 0''.42$ (P.A. = 49°) and $0''.60 \times 0''.44$ (P.A. = 46°) for the continuum image and the H_2CO image, respectively. The rms noise levels are 1 and 10 mJy $beam^{-1}$ for the continuum and the H_2CO emission, respectively. The continuum emission has its peak intensity at: $(\alpha_{2000}, \delta_{2000}) = (15^h43^m02^s.24, -34°09'06''.7)$. The CCH data were combined with those taken in another ALMA observation program (2011.0.00628.S; PI: Jes Jørgensen), which was carried out with 15 − 16 antennas. The signal-to-noise ratio (S/N) was improved from 13.7 to 24.5 by this combination. The synthesized beam

Table 5.1 Observed Line Parameters[a]

Molecule	Transition	Frequency (GHz)	$E_u k_B^{-1}$ (K)	$S\mu^2$[b] (D^2)
H_2CO	$5_{0,5} - 4_{0,4}$	362.7360480	52	27.168
	$5_{1,5} - 4_{1,4}$	351.7686450	62	26.096
	$5_{2,4} - 4_{2,3}$	363.9458940	100	22.834
CCH	$N = 4 - 3$, $J = 7/2 - 5/2$, $F = 3 - 2$	349.4006712	42	1.6942
	$N = 4 - 3$, $J = 7/2 - 5/2$, $F = 4 - 3$	349.3992756	42	2.2712

[a] Taken from CDMS [15]
[b] Nuclear spin degeneracy is not included.

of the combined CCH image is $0''.70 \times 0''.46$ (P.A. $= 72°$). Its rms noise level is 15 mJy beam^{-1}. No other significant line features were detected in these observations, except for the line emissions reported by [7].

5.3 Results

5.3.1 Overall Distribution of H_2CO and CCH

Figure 5.1a shows the moment 0 (integrated intensity) map of the H_2CO ($5_{1,5} - 4_{1,4}$) line. A well-collimated outflow is detected prominently, symmetrically extending along the northeast-southwest axis from the protostellar position. The wall of this outflow has a straight structure, as like as the outflow of HH46 [1]. Figure 5.1b shows the velocity map (moment 1 map), showing that the northeastern and southwestern outflow lobes are red-shifted and blue-shifted, respectively. In these observations, the emission extending over $12''$ scale or larger would be affected by the resolving-out effect due to the lack of short baseline data. Although the size of the detected outflow is as compact as $8''$ for each lobe, the emission from the outer part may be resolved out. As well, it may be weak due to insufficient excitation conditions for the observed molecular lines. At a distance of $8''$ from the protostellar position, the apparent width of the outflow is about $4''$. Figure 5.1c shows the integrated intensity map (moment 0 map) of the high-excitation H_2CO ($5_{2,4} - 4_{2,3}$) line. The emitting region of the H_2CO ($5_{2,4} - 4_{2,3}$) line is essentially similar to that of the H_2CO ($5_{1,5} - 4_{1,4}$) line, although the S/N ratio is rather poor for the former line. In these maps, a bright knot is detected in the red-shifted lobe ('Clump A' in Fig. 5.1a). This component could be a shocked region caused by an impact of the outflow with dense clumps in the surrounding cloud.

As well as the outflow, a single-peaked compact component is also recognized in the vicinity of the protostar in Fig. 5.1d (a blow-up of the central part of Fig. 5.1a).

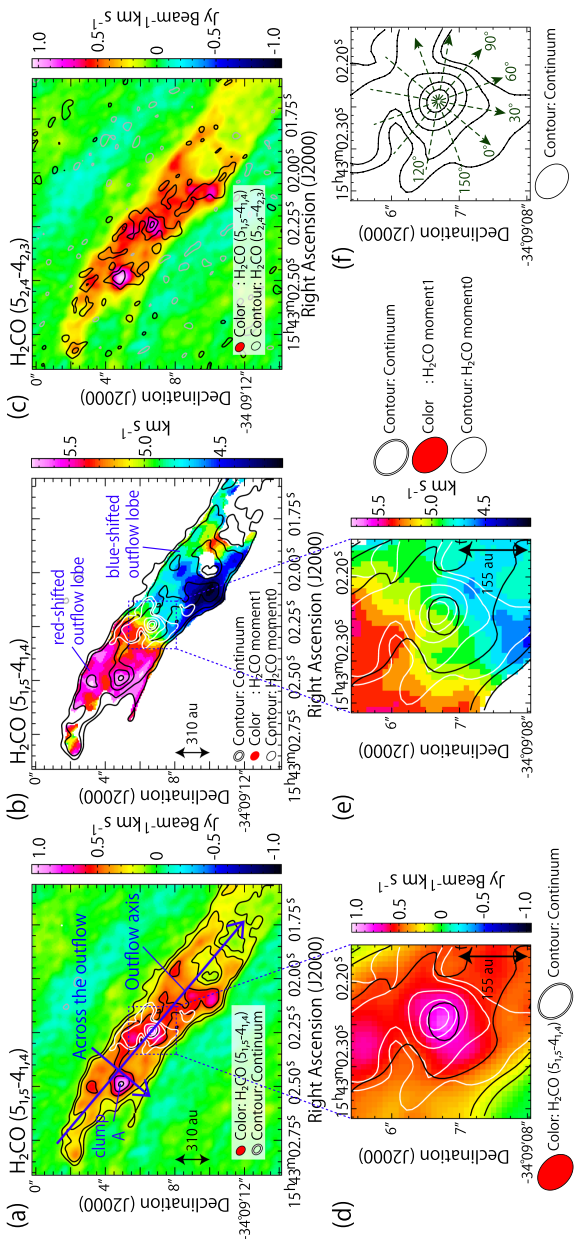

Fig. 5.1 **a** Integrated intensity map (moment 0) of the H_2CO ($5_{1,5} - 4_{1,4}$) line (color; black contours). White contours show the 0.8 mm continuum emission. The PV diagrams in Figs. 5.5a, b are prepared along the blue arrows. **b** Velocity map (moment 1 map) of the H_2CO ($5_{1,5} - 4_{1,4}$) line. Black and white contours are the same as those in panel (**a**). **c** Integrated intensity map of the H_2CO ($5_{2,4} - 4_{2,3}$; contours) line. The color map is the same as that in panel (**a**). A few bright spots are seen in the both lines of H_2CO. **d** A blow-up of the integrated intensity map of the H_2CO ($5_{1,5} - 4_{1,4}$) line (panel **a**) in the vicinity of the protostar. **e** A blow-up of the velocity map of the H_2CO ($5_{1,5} - 4_{1,4}$) line (panel **b**) in the vicinity of the protostar. **f** A blow-up of the 0.8 mm continuum map in the vicinity of the protostar. The PV diagrams in Figs. 5.7, 5.9, and 5.10 are prepared along the dashed arrows. The arrow labeled as "0°" has the position angle (P.A.) of 140°, and others are taken for P.A. of every 30°.

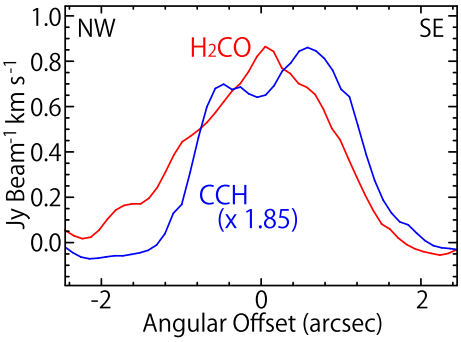

Fig. 5.2 Intensity profiles of the H_2CO ($5_{1,5} - 4_{1,4}$) line and the CCH ($N = 4 - 3$, $J = 7/2 - 5/2$, $F = 4 - 3$ and $3 - 2$) lines along the line perpendicular to the outflow axis ("0°" shown in Fig. 5.1f)

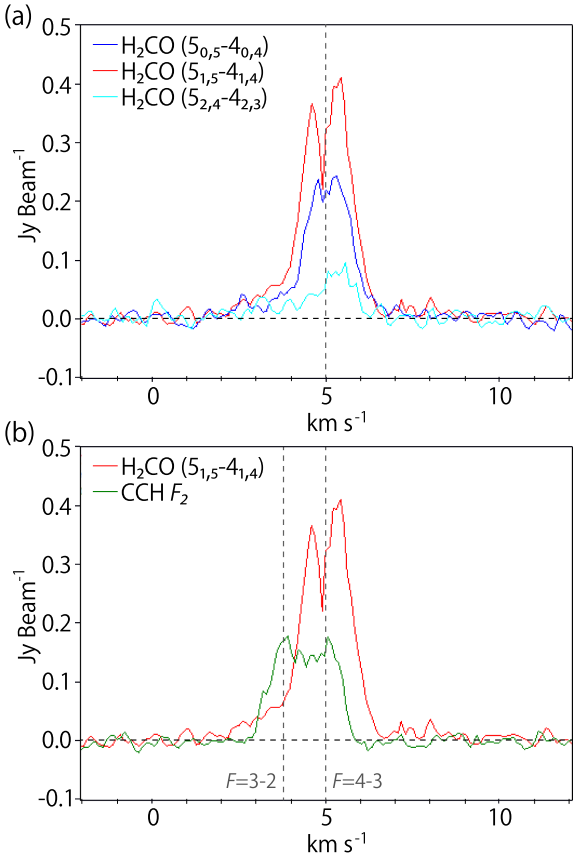

Fig. 5.3 Spectra of the H_2CO ($5_{0,5} - 4_{0,4}$, $5_{1,5} - 4_{1,4}$ and $5_{2,4} - 4_{2,3}$) lines and the CCH ($N = 4 - 3$, $J = 7/2 - 5/2$, $F = 4 - 3$ and $3 - 2$) lines prepared toward the protostellar position. In panel (**b**), the systemic velocities for the two hyperfine components of CCH are represented by the two vertical dashed lines

Figure 5.1e represents a blow-up of the velocity map (Fig. 5.1b). The approximate extent of the central component is estimated to be about 2″ (310 au) in diameter based on the spatial profile of the line intensity prepared along the line perpendicular to the outflow axis (Fig. 5.2). In Fig. 5.3, the spectral line profiles of the H_2CO and CCH

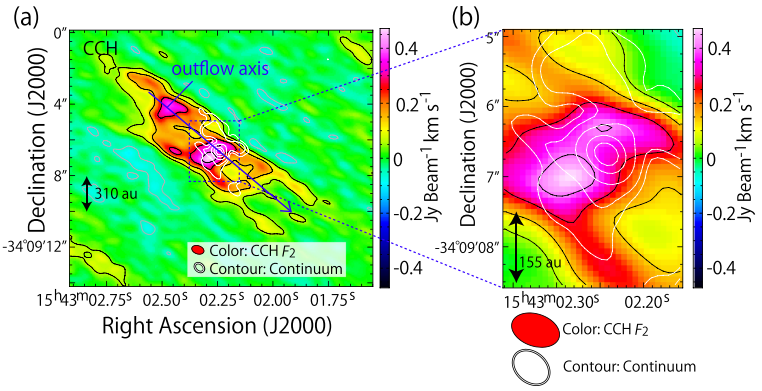

Fig. 5.4 **a** Integrated intensity map of the CCH ($N = 4 - 3$, $J = 7/2 - 5/2$, $F = 4 - 3$ and $3 - 2$; color, black contour) lines. White contours represent the 0.8 mm continuum map as the same as those in Fig. 5.1a. The PV diagram in Fig. 5.6 is prepared along the blue arrow parallel to the outflow axis. **b** A blow-up of panel (**a**) in the vicinity of the protostar. Contours are as the same as those in panel (**a**)

lines are shown, which are prepared at the protostellar position and averaged over the beam size. The line width of the H_2CO line is as narrow as 2 km s^{-1} even toward the protostellar position. By using the RADEX program [29] to fit the intensity of the two temperature sensitive lines of para-H_2CO ($5_{0,5} - 4_{0,4}$, $5_{2,4} - 4_{2,3}$), the column density of H_2CO and its kinetic temperature toward the protostellar position are estimated to be 3×10^{13} cm^{-2} and $36 - 38$ K, respectively, assuming the H_2 density of $(1 \times 10^7 - 1 \times 10^8)$ cm^{-3} and the line width of 1.8 km s^{-1} for the H_2CO line. As well, the ortho/para ratio is estimated to be 2.8 based on the intensity of the ortho-H_2CO ($5_{1,5} - 4_{1,4}$) line. The optical depths for these lines are 0.27 ($5_{0,5} - 4_{0,4}$), 0.06 ($5_{2,4} - 4_{2,3}$), 0.53 ($5_{1,5} - 4_{1,4}$), and therefore, the lines are not opaque.

The integrated intensity map of the CCH ($N = 4 - 3$, $J = 7/2 - 5/2$, $F = 4 - 3$ and $3 - 2$) lines is shown in Fig. 5.4a, and its blow-up is in Fig. 5.4b. The outflow cavity is prominently traced as well as the centrally concentrated component is also seen. The emitting region of the CCH line around the protostar is more extended along the southeast-northwest axis than that of the H_2CO line. The CCH emission shows a slight dip toward the protostellar position, as shown in its intensity profile prepared along the line perpendicular to the outflow axis (Fig. 5.2). This feature is consistent with the previous report [7]. The spectrum of the CCH lines taken at the protostellar position is complicated due to the two hyperfine components (Fig. 5.3). Nevertheless, the line width of each hyperfine component of CCH is found to be 2 km s^{-1} or less, as like as that of the H_2CO line.

5.3.2 *Outflow*

First, the outflow feature detected in the H_2CO ($5_{1,5} - 4_{1,4}$) line is analyzed. Figure 5.5a shows the position-velocity (PV) diagram of the H_2CO ($5_{1,5} - 4_{1,4}$) line. Its position axis is shown by a blue arrow in Fig. 5.1a, which is centered at the protostellar position and prepared along the outflow axis. The observed outflow structure extends along the northeast-southwest axis from the protostellar position, where the northeastern and southwestern parts are red-shifted and blue-shifted, respectively. Since the red-shifted and blue-shifted outflow lobes show little overlap with each other near the protostar, the outflow likely blows almost perpendicular to the plane of the sky, which indicates that the disk/envelope geometry has a nearly edge-on configuration. As often observed for outflow cavities (e.g. [1, 10]), the highest velocity shift in Fig. 5.5a is found to increase linearly as the distance from the protostar. An intense knot is detected in the red-shifted component, corresponding to Clump A in the integrated intensity map (Fig. 5.1a). As well as the high velocity-shift components, other components are found near the systemic velocity (~ 5 km s^{-1}; [22]). The low velocity-shift components are slightly blue-shifted and red-shifted on the northeastern and southwestern side of the protostar. This trend is the opposite case to the high velocity-shift components.

Figure 5.5b shows the PV diagram of the H_2CO ($5_{1,5} - 4_{1,4}$) line in the red-shifted outflow lobe, whose position axis is prepared to be perpendicular to the outflow axis as shown in Fig. 5.1a. This diagram shows an elliptic feature. As well, a knot-like emission is also detected in the higher-velocity range. This emission corresponds to Clump A found in the integrated intensity map (Fig. 5.1a). The velocity structure shown in the PV diagram likely suggests the expanding motion of the gas in the outflow cavity wall.

In this study, the standard model of an outflow cavity from [10] is employed to analyze the observed geometrical and kinematical structures of the outflow, which

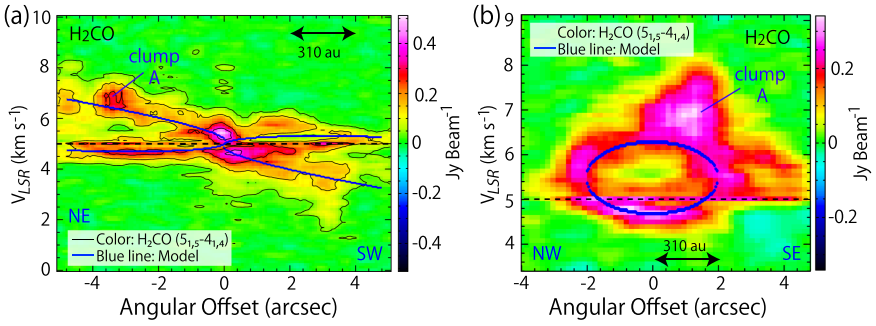

Fig. 5.5 PV diagrams of the H_2CO ($5_{1,5} - 4_{1,4}$) line **a** along the outflow axis and **b** the line perpendicular to it. Their position axes are represented by the blue arrows in Fig. 5.1a. Blue lines show the best outflow model with an inclination angle of 70° (0° for a pole-on configuration). The systemic velocity is represented by the black horizontal line in each panel

is employed for the outflow analysis in L1527 (Chap. 4). In this model, a parabolic shape is assumed for the outflow cavity wall, and the velocity of the gas on the wall is assumed to be proportional to the distance to the protostar;

$$z = C_{\rm as} R^2, \quad v_R = v_{\rm as} \frac{R}{R_0}, \quad v_z = v_{\rm as} \frac{z}{z_0}, \tag{5.1}$$

where z denotes the distance to the protostar along the outflow axis, and R the radial size of the cavity wall perpendicular to z-axis (see Chap. 3). Both z_0 and R_0 are normalization constants set to be $1''$. $C_{\rm as}$ and $v_{\rm as}$ are free parameters. In this model, the intensity of the emission is assumed to be proportional to the column density, where the molecular density is simply assumed to be constant. These assumptions may not be realistic. However, they do not matter the following analysis, because this study focuses on the velocity structure but not on the intensity profile. The best results are obtained with an inclination angle of 70° (0° for a pole-on configuration), as represented by the blue lines in Fig. 5.5. With an inclination angle less than 60° or higher than 80°, the outflow model does not reproduce the observed kinematic structure well with any values of $C_{\rm as}$ and $v_{\rm as}$. Hence, the inclination angle is determined to be 70° ± 10°, where the error value is the estimated limit based on the above results. The derived parameters are $C_{\rm as}$ of 0.8 arcsec^{-1} and $v_{\rm as}$ of 0.38 km s^{-1} for an inclination angle of 70°. As mentioned in Sect. 5.1, [30] reported an inclination angle of 15°, a nearly pole-on geometry. This discrepancy seems to originate from the limited spatial resolution of their data. Another possibility is that the outflow direction at a small scale is different from that on larger scales (e.g. [8, 14, 20, 32]), as discussed in the analysis of L1527 (Cha. 4). On the other hand, Atacama Pathfinder EXperiment observations of the CO ($J = 6 - 5$) line indicate an inclination angle of 70° [31], which is consistent with the above result.

Figure 5.6 shows the PV diagram of the CCH ($N = 4 - 3$, $J = 7/2 - 5/2$, $F = 4 - 3$ and $3 - 2$) line prepared along the outflow axis through the protostellar position. The appearance of the PV diagram is complicated due to the two hyperfine components blending with a separation of only 1.2 km s^{-1}. Compared with the H_2CO case, the low velocity-shift components of CCH is relatively bright in comparison with its high velocity-shift components. This suggests that the CCH emission from the outflow component primarily traces the compressed ambient gas around the outflow cavity rather than the entrained outflowing gas. Gas-phase reactions in dense photodissociation region layers may form CCH (e.g. [5, 6, 26]).

5.3.3 *Protostellar Envelope*

A centrally concentrated component is detected in both the H_2CO and CCH emission (Figs. 5.1d, 5.4b). The distributions of $C^{34}S$, $C^{17}O$, and CH_3OH also have such a component [7]. In this section, the kinematic structure of this component is investigated. A blow-up of the velocity map of the H_2CO line (Fig. 5.1e) is dominated by

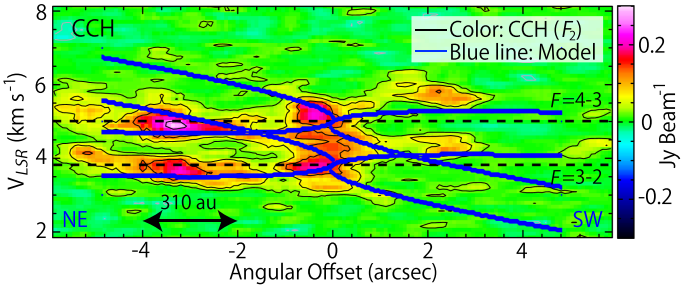

Fig. 5.6 PV diagram of the CCH ($N = 4 - 3$, $J = 7/2 - 5/2$, $F = 4 - 3$ and $3 - 2$) lines. The position axis is taken along the outflow axis, which is shown by a blue arrow in Fig. 5.4a. Blue lines in the diagram represent the outflow model results with an inclination angle of 70°, which is the best model obtained in the H_2CO analysis (Sect. 5.3.2). The systemic velocities for the two hyperfine components of CCH (5.0 km s^{-1}, 3.8 km s^{-1}) are shown by the black dashed lines

the overwhelming emission from the outflow components. Nevertheless, a slightly skewed feature is marginally recognized around the continuum peak position. In order to reveal the gas motion in the vicinity of the protostar more carefully, PV diagrams around the protostar are prepared (Fig. 5.7).

The PV diagrams of the H_2CO ($5_{1,5} - 4_{1,4}$) line are shown in Fig. 5.7a, b. They are prepared along the lines shown in Fig. 5.1f, centered at the protostellar position; Fig. 5.7a is along the line perpendicular to the outflow axis ("0°"), while Fig. 5.7b along the outflow axis ("90°"). Although a rotation signature is not obvious in the centrally concentrated component in Fig. 5.7a, there is a marginal trend that the intensity peaks in the red-shifted and the blue-shifted velocity ranges are on the southeastern and northwestern sides of the protostellar position, respectively. In fact, this rotation motion has been later confirmed [17].

Meanwhile, Fig. 5.7b shows two intensity peaks in the vicinity of the protostar; one on the northeastern side of the protostar is red-shifted, the other on the southwestern side is blue-shifted. This systematic velocity gradient is the same case of that found in the outflow (Fig. 5.5a). However, the modest velocity gradient near the protostar is difficult to attribute to the outflow component, according to the outflow model result obtained in Sect. 5.3.2. Based on the outflow direction and its inclination angle, the outflow and disk/envelope structure of IRAS 15398−3359 is schematically illustrated as shown in Fig. 5.8. Therefore, the velocity gradient found in Fig. 5.7b is likely a signature of an infall motion of the envelope gas rather than an outflow motion.

An infall/rotation signature is not clearly seen in the PV diagrams for the CCH ($N = 4 - 3$, $J = 7/2 - 5/2$, $F = 4 - 3$ and $3 - 2$) lines (Fig. 5.7c, d), in contrast to the L1527 case (Chapters 3, 4 [21, 23]). In L1527, whose protostellar mass and inclination angle are derived to be 0.18 $M_\odot$ and 85°, respectively, the observed velocity shift of the CCH line is 1.8 km s^{-1} at a radius of 100 au from the protostar. On the contrary, the velocity shifts are as small as 1 km s^{-1} and 0.7 km s^{-1} in the H_2CO and CCH lines, respectively, in IRAS 15398−3359 (Fig. 5.7), although a nearly edge-

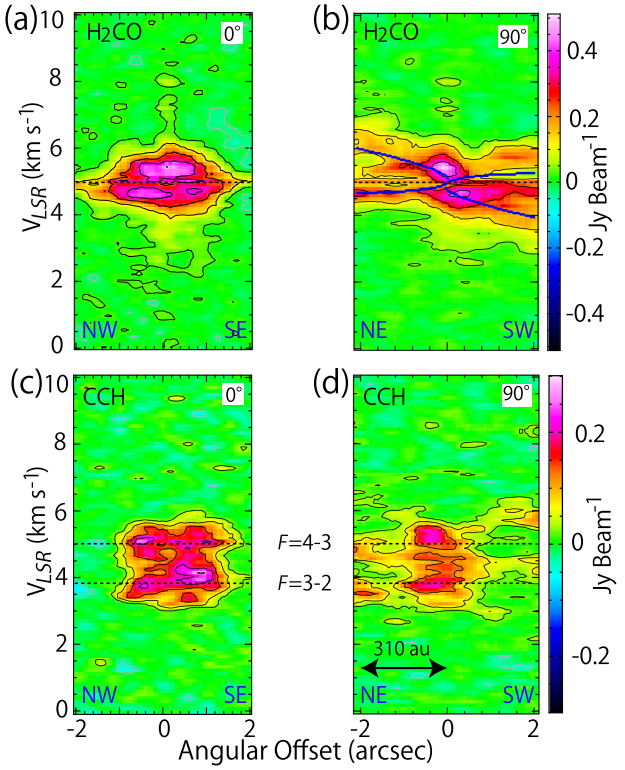

Fig. 5.7 PV diagrams of the H_2CO ($5_{1,5} - 4_{1,4}$; a, b) and CCH ($N = 4 - 3$, $J = 7/2 - 5/2$, $F = 4 - 3$ and $3 - 2$; c, d) lines. Their position axes are shown in Fig. 5.1f; those for panels (**a**) and (**c**) are taken along the line perpendicular to the outflow axis ("0°"), while those for (**b**) and (**d**) are along the outflow axis ("90°"). Panels (**b**) and (**d**) are blow-ups of Figs. 5.5a and 5.6, respectively. Blue lines in panel (**b**) represent the best model for the outflow component (Sect. 5.3.2)

on configuration (70°; 0° for a face-on configuration) is expected according to the outflow analysis (Sect. 5.3.2). Although IRAS 15398−3359 is similar to L1527 in its large-scale (∼ a few 1000 au) chemical composition [22], infall/rotation motions are not very clear contrarily.

In these observations, the structure down to 78 au (0.″5) are resolved around the protostar. Nevertheless, the observed line widths are quite narrow. Considering the nearly edge-on configuration, it is suggested that the Doppler shift due to infall/rotation motions around the protostar is small. A small velocity-shift could be explained if the observed dense gas were not associated with the protostar, that is, if it were mostly present in the outflow component. However, this is not likely the case because the modeled outflow motion does not well explain the velocity gradient traced by the H_2CO line (Fig. 5.7b), as mentioned above. Hence, the small velocity-shift likely implies a low protostellar mass. A rough upper limit for the protostellar mass is estimated based on the maximum value of the observed velocity shifts. Under

the conservation law of energy, the protostellar mass (M) is represented in terms of the infall velocity ($v_{\rm infall}$) and the rotation velocity ($v_{\rm rotation}$) as:

$$M = \frac{r}{2G}\left(v_{\rm infall}^2 + v_{\rm rotation}^2\right), \tag{5.2}$$

where r denotes the distance to the protostar. By using this relation, the protostellar mass is roughly estimated to be smaller than 0.09 $M_\odot$ with a maximum velocity less than 1 km s^{-1} at 0.″5 (78 au) from the protostar. Here, both the infall and rotation velocities are assumed to be the observed maximum value of 1 km s^{-1} in Fig. 5.7a as a robust case. If there is no rotation motion, i.e. the free fall case, the upper limit for the protostellar mass is obtained to be 0.04 $M_\odot$. This rough estimate is indeed consistent with the later report with a further observation [17].

5.3.4 Comparison with an Envelope Model

A ballistic model of an infalling-rotating envelope (Fig. 5.8) is employed to investigate the observational results of the c-C_3H_2 and CCH lines toward L1527 (Chaps. 3

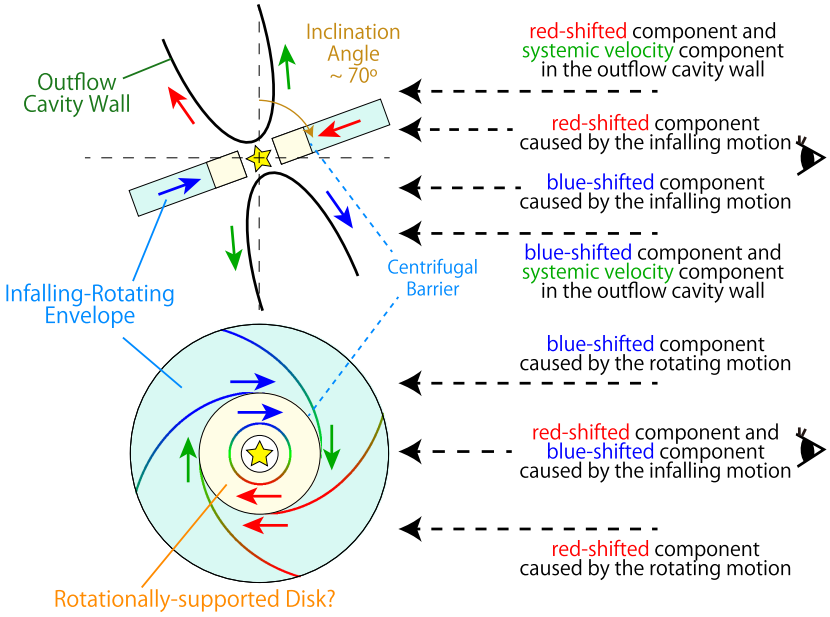

Fig. 5.8 Schematic illustrations of the outflow and disk/envelope system. An observer sits on the right hand side, whose line of sight is shown by the black dashed arrows. The disk/envelope system has an almost edge-on geometry with an inclination angle of 70° (0° for a face-on configuration)

and 4). This source has similar chemical characteristics to IRAS 15398−3359. In spite of the simplicity of this model, the basic features of the PV diagrams of the c-C_3H_2 and CCH lines toward L1527 are well reproduced. Therefore, it is worth applying the same model to the kinematic structure traced by the H_2CO and CCH lines in IRAS 15398−3359. The CCH emission observed in L1527 only traces the infalling-rotating envelope, and thus, it is preferable to apply the infalling-rotating envelope model for the CCH line. However, the PV diagrams of different transitions of CCH observed toward IRAS 15398−3359 are complicated due to the hyperfine structure, and their signal-to-noise ratios are insufficient for critical comparison. In contrast, the H_2CO ($5_{1,5} - 4_{1,4}$) emission is bright enough in IRAS 15398−3359. Although H_2CO possibly resides in the inner disk-like structure in addition to the infalling-rotating envelope, the contribution of the envelope seems significant in L1527 [21]. Hence, the model results are compared with the H_2CO ($5_{1,5} - 4_{1,4}$) line observed in IRAS 15398−3359.

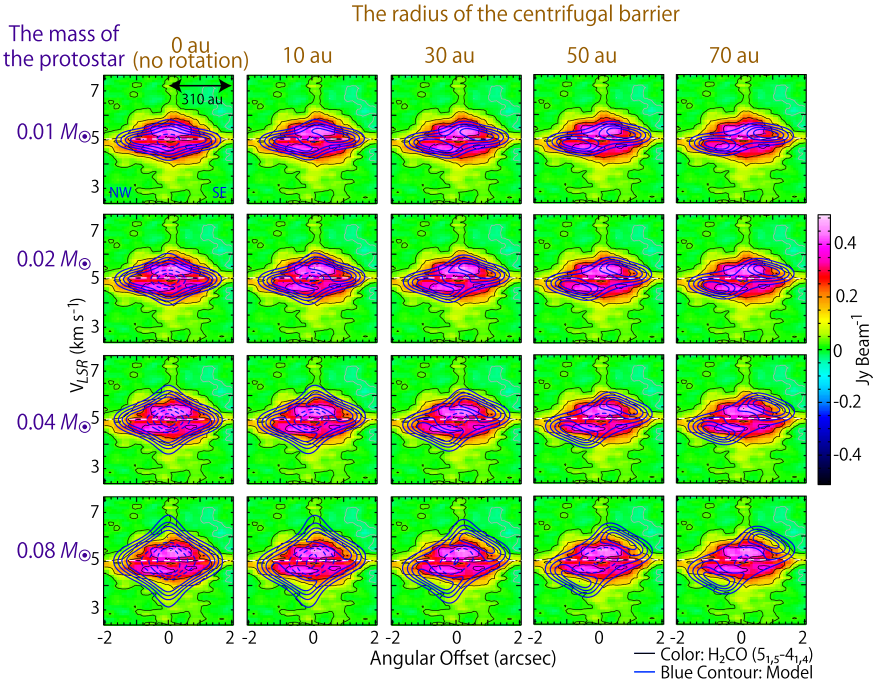

Fig. 5.9 PV diagrams of the H_2CO ($5_{1,5} - 4_{1,4}$) line prepared along the line perpendicular to the outflow axis. Their position axes are represented by the arrow labeled as "0°" in Fig. 5.1f. Blue contours represent 20 model results of the infalling-rotating envelope with an inclination angle of 70°. The protostellar mass and the radius of the centrifugal barrier are varied as free parameters (see Chap. 3). Contour levels are every 20% of the peak intensity in each panel. Dashed contours around the central position represent the intensity dip

Figure 5.9 shows the PV diagrams of the H_2CO ($5_{1,5} - 4_{1,4}$) line along the line perpendicular to the outflow axis (the arrow labeled as "0°" in Fig. 5.1f), that is, along the mid-plane of the envelope. The blue contours represent the results of the infalling-rotating envelope model. In this model, the intensity is simply assumed to be proportional to the column density. The molecular density is assumed to be proportional to $r^{-1.5}$, where r denotes the distance to the protostar. The assumption of the optically thin condition seems to be reasonable, because the optical depth is evaluated to be less than 0.3 (Sect. 5.3.1). The excitation effect and the effect of the temperature gradient are not taken into account, neither. However, these simplifications may not affect the following analysis, because this analysis only focuses on the velocity structure but not on the intensity profile. In contrast to the L1527 case (Chap. 4), the radius of the centrifugal barrier cannot be directly determined from the PV diagram because of the absence of an obvious rotation signature. Nevertheless, its upper limit can be roughly estimated based on the CCH distribution. If CCH resides only in the infalling-rotating envelope as in the case of L1527 and the radius of the centrifugal barrier is larger than the beam size, a hole in the CCH distribution toward the protostellar position is expected to be resolved. Although an intensity dip toward the protostar is marginally seen in the CCH emission (Fig. 5.2), this feature is not well resolved in the present observation with the beam size of 0.″5 (78 au). Hence, the upper limit for the centrifugal barrier is set to be 80 au. Under this constraint, Fig. 5.9 shows the simulated PV diagrams of the infalling-rotating envelope models with various sets of the protostellar mass (M) and the radius of the centrifugal barrier (r_{CB}). Among the 20 models in Fig. 5.9, ones with M of 0.02 $M_\odot$ and r_{CB} from 0 to 30 au are chosen as the best models by eye. The value of M is consistent with its upper limit obtained in Sect. 5.3.3. Thus, the low protostellar mass of this source is confirmed with this model analysis. The PV diagrams of the model and observation along the different directions are also shown in Fig. 5.10; the diagrams are prepared along the six lines shown in Fig. 5.1f, and the model with M of 0.02 $M_\odot$ and r_{CB} of 30 au are employed as an example. The observed trends of velocity gradients around the protostar seem to be explained by this model.

5.4 Discussion

The small protostellar mass of IRAS 15398−3359 ($< 0.09\ M_\odot$) is essentially derived from the narrow line width detected in the inner envelope (< 80 au) with an almost edge-on configuration (70°; 0° for a face-on configuration). The mass estimates may suffer from the uncertainty in the inclination angle of the disk/envelope system, since the inclination angle evaluated for the outflow structure is employed as the substitute. If the inclination angle is smaller than the employed value, i.e. nearer to the face-on configuration, the mass evaluation by the model increases. Nevertheless, the upper limit value for the protostellar mass does not change significantly, even if an inclination angle of 60° is employed. In fact, the upper limit value was confirmed

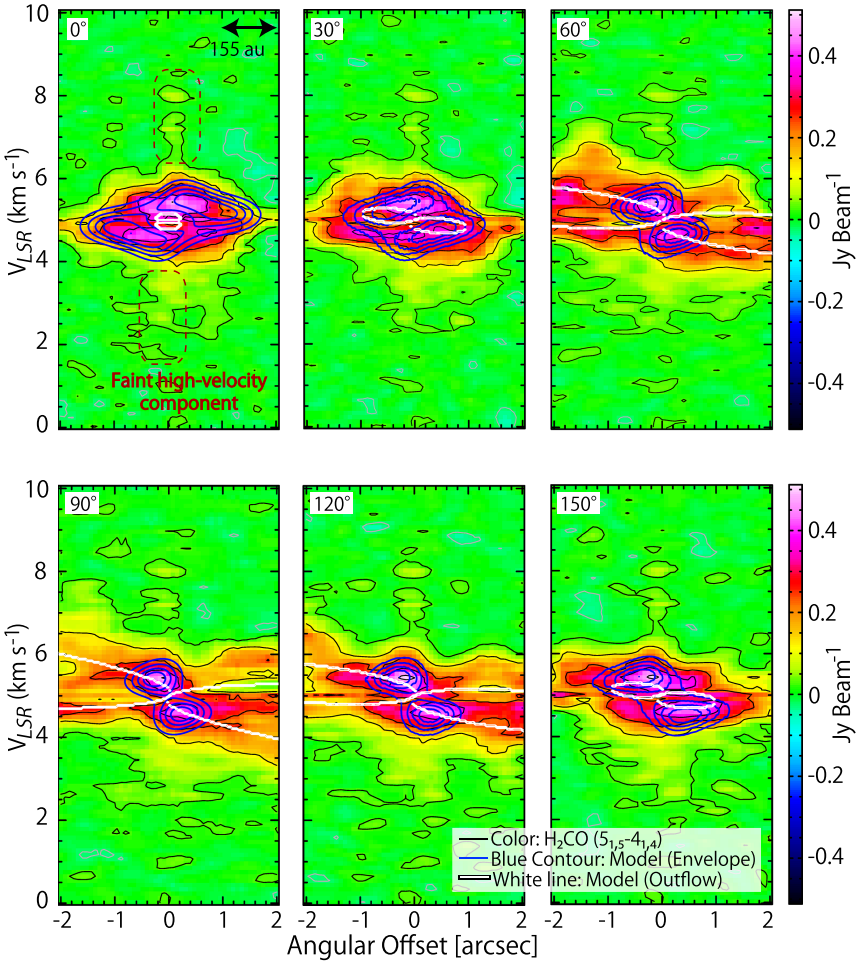

Fig. 5.10 PV diagrams of the H_2CO ($5_{1,5} - 4_{1,4}$) line prepared centered at the protostellar position. Their position axes are represented by the six arrows in Fig. 5.1f, which are taken for different position angles. Blue contours represent the results of the infalling-rotating envelope model. The parameters for the model are the inclination angle of 70°, the protostellar mass of 0.02 $M_\odot$, and the radius of the centrifugal barrier of 30 au. Contour levels are every 20% of the peak intensity in each panel. White lines show the outflow model obtained in Sect. 5.3.2

to be adequate later based on the further observations [17], where the protostellar mass was evaluated to be as small as 0.007 $M_\odot$.

The averaged accretion rate is evaluated to be less than 9.0×10^{-5} $M_\odot$ yr^{-1} by using the dynamical timescale of the extended outflow ($(1 - 2) \times 10^3$ yr for each lobe [31]) and the upper limit for the protostellar mass (< 0.09 $M_\odot$) obtained in Sect. 5.3.3. Because older parts of the outflow structure may not be detected, the

evaluated dynamical timescale of the outflow should be regarded as its lower limit. Thus, the above value for the averaged accretion rate is its upper limit. Nevertheless, the estimated accretion rate seems roughly consistent with the typical value for low-mass protostars from 10^{-5} to 10^{-6} $M_\odot$ yr^{-1} (e.g. [4]), and may be higher than that for another WCCC source L1527 (10^{-6} $M_\odot$ yr^{-1} [16]). Meanwhile, the mass outflow rate is calculated to be 6.3×10^{-6} $M_\odot$ yr^{-1} and 2.2×10^{-6} $M_\odot$ yr^{-1} for the red- and blue-shifted lobes, respectively, by using their masses and dynamical timescales reported by [30]. These values are modified to be 1.7×10^{-5} $M_\odot$ yr^{-1} and 6.2×10^{-6} $M_\odot$ yr^{-1} including the correction for the inclination angle of 70°. Therefore, the averaged mass accretion rate and the mass outflow rate seem to be roughly comparable to each other.

Meanwhile, the mass accretion rate ($\dot{M}$) can be estimated by using the following equation [19]:

$$\dot{M} = \frac{L R_{\rm star}}{G M}, \tag{5.3}$$

where M, L, and $R_{\rm star}$ denote the mass, luminosity, and radius of the protostar, respectively. With the upper limit for M (< 0.09 $M_\odot$) obtained in Sect. 5.3.3, $\dot{M}$ is estimated to be larger than 1.6×10^{-6} $M_\odot$ yr^{-1} by employing L of 1.8 $L_\odot$ [7] and $R_{\rm star}$ of 2.5 $R_\odot$ (e.g. [2, 18]). This lower limit value for $\dot{M}$ is consistent with its upper limit obtained above (9.0×10^{-5} $M_\odot$ yr^{-1}). In spite of the episodic accretion in this source suggested by [7], the averaged mass accretion rate does not significantly differ from the canonical value ($10^{-5} - 10^{-6}$ $M_\odot$ yr^{-1}).

The upper limit of the protostar/envelope mass ratio is evaluated to be 0.18 by using the upper limit for the protostellar mass of 0.09 $M_\odot$ and an envelope mass of 0.5 $M_\odot$ [9]. Employing the protostellar mass of 0.02 $M_\odot$, the ratio is calculated to be 0.04. Thus, the ratio in this source seems smaller than that in L1527 (0.2 [28]). This result implies that the protostar is in its infant stage and is still growing, which was later supported with further investigation [17]. Since the specific angular momentum of the gas brought into the vicinity of the protostar is expected to be smaller at the earlier stage in the protostar evolution, it would be a natural consequence that the rotation signature is not evident in IRAS 15398−3359 in contrast to the case in L1527 (Chap. 4), a more evolved Class I source.

In Fig. 5.2, the H_2CO emission shows a centrally concentrated distribution with a single peak, whereas the CCH emission has a more flattened distribution. Therefore, the H_2CO emission is expected to trace the inner region than the CCH emission. A similar trend is also seen in L1527 [21]. It should be noted that Fig. 5.10 shows a faint high-velocity component of H_2CO ($v_{\rm lsr} < 4$ km s^{-1} or $v_{\rm lsr} > 6$ km s^{-1}) toward the protostellar position. If this faint emission is really the contribution from a rotationally-supported disk, it means that a disk structure is already formed at such a very early stage of the low-mass star-formation. With the upper limit for the protostellar mass of 0.09 $M_\odot$, the maximum velocity shift about 3 km s^{-1} in the H_2CO line corresponds to the radius of 10 au.

As demonstrated in this chapter, extensive studies of the disk/envelope structure in a Class 0 source have now become possible with ALMA, and a chemical approach

is helpful for such studies. This study reveals that the disk/envelope structure can be traced with various molecular lines. Hence, the chemical evolution can be addressed even in the disk-forming stage.

References

1. Arce HG, Mardones D, Corder SA, Garay G, Noriega-Crespo A, Raga AC (2013) ALMA observations of the HH 46/47 molecular outflow. ApJ 774(1):39
2. Baraffe I, Chabrier G (2010) Effect of episodic accretion on the structure and the lithium depletion of low-mass stars and planet-hosting stars. A&A 521:A44
3. Brinch C, Jørgensen JK, Hogerheijde MR (2009) The kinematics of NGC 1333-IRAS2A - a true Class 0 protostar. A&A 502(1):199–205
4. Hartmann L, Cassen P, Kenyon SJ (1997) Disk accretion and the stellar birthline. ApJ 475(2):770–785
5. Jansen DJ, Spaans M, Hogerheijde MR, van Dishoeck EF (1995) Millimeter and submillimeter observations of the Orion Bar. II. Chemical models. A&A 303:541
6. Jansen DJ, van Dishoeck EF, Black JH, Spaans M, Sosin C (1995) Physical and chemical structure of the IC 63 nebula. II. Chemical models. A&A 302:223
7. Jørgensen JK, Visser R, Sakai N, Bergin EA, Brinch C, Harsono D, Lindberg JE, van Dishoeck EF, Yamamoto S, Bisschop SE, Persson MV (2013) A recent accretion burst in the low-mass protostar IRAS 15398–3359: ALMA imaging of its related chemistry. ApJ 779(2):L22
8. Kristensen LE, Klaassen PD, Mottram JC, Schmalzl M, Hogerheijde MR (2013) ALMA CO J = 6–5 observations of IRAS 16293–2422. Shocks and entrainment. A&A 549:L6
9. Kristensen LE, van Dishoeck EF, Bergin EA, Visser R, Yıldız UA, San Jose-Garcia I, Jørgensen JK, Herczeg GJ, Johnstone D, Wampfler SF, Benz AO, Bruderer S, Cabrit S, Caselli P, Doty SD, Harsono D, Herpin F, Hogerheijde MR, Karska A, van Kempen TA, Liseau R, Nisini B, Tafalla M, van der Tak F, Wyrowski F (2012) Water in star-forming regions with Herschel (WISH). II. Evolution of 557 GHz 1_{10}-1_{01} emission in low-mass protostars. A&A 542:A8
10. Lee C-F, Mundy LG, Reipurth B, Ostriker EC, Stone JM (2000) CO outflows from young stars: confronting the jet and wind models. ApJ 542(2):925–945
11. Lombardi M, Lada CJ, Alves J (2008) Hipparcos distance estimates of the Ophiuchus and the Lupus cloud complexes. A&A 480(3):785–792
12. Mardones D, Myers PC, Tafalla M, Wilner DJ, Bachiller R, Garay G (1997) A search for infall motions toward nearby young stellar objects. ApJ 489(2):719–733
13. Maret S, Belloche A, Maury AJ, Gueth F, André P, Cabrit S, Codella C, Bontemps S (2014) First results from the CALYPSO IRAM-PdBI survey. I. Kinematics of the inner envelope of <ASTROBJ>NGC 1333-IRAS2A</ASTROBJ>. *A&A*, 563:L1
14. Mizuno A, Fukui Y, Iwata T, Nozawa S, Takano T (June 1990) A remarkable multilobe molecular outflow: rho ophiuchi east, associated with IRAS 16293–2422. ApJ 356:184
15. Müller HSP, Schlöder F, Stutzki J, Winnewisser G (2005) The cologne database for molecular spectroscopy, CDMS: a useful tool for astronomers and spectroscopists. J Molecular Struct 742(1-3):215–227
16. Ohashi N, Hayashi M, Ho PTP, Momose M (1997) Interferometric imaging of IRAS 04368+2557 in the L1527 molecular cloud core: a dynamically infalling envelope with rotation. ApJ 475(1):211–223
17. Okoda Y, Oya Y, Sakai N, Watanabe Y, Jørgensen JK, Van Dishoeck EF, Yamamoto S (2018) The co-evolution of disks and stars in embedded stages: the case of the very-low-mass protostar IRAS 15398–3359. ApJ 864(2):L25

18. Palla F (1999) The evolution of pre-main-sequence stars. In: Lada CJ, Kylafis ND (eds) The origin of stars and planetary systems, volume 540 of NATO Advanced Study Institute (ASI) series C, p 375
19. Palla F, Stahler SW (1991) The evolution of intermediate-mass protostars. I. Basic results. ApJ 375:288
20. Sakai N, Ceccarelli C, Bottinelli S, Sakai T, Yamamoto S (2012) Distribution of CH_3OH in NGC 1333 IRAS4B. ApJ 754(1):70
21. Sakai N, Oya Y, Sakai T, Watanabe Y, Hirota T, Ceccarelli C, Kahane C, Lopez-Sepulcre A, Lefloch B, Vastel C, Bottinelli S, Caux E, Coutens A, Aikawa Y, Takakuwa S, Ohashi N, Yen H-W, Yamamoto S (2014) A chemical view of protostellar-disk formation in L1527. ApJ 791(2):L38
22. Sakai N, Sakai T, Hirota T, Burton M, Yamamoto S (2009) Discovery of the second warm carbon-chain-chemistry source, IRAS15398 - 3359 in lupus. ApJ 697(1):769–786
23. Sakai N, Sakai T, Hirota T, Watanabe Y, Ceccarelli C, Kahane C, Bottinelli S, Caux E, Demyk K, Vastel C, Coutens A, Taquet V, Ohashi N, Takakuwa S, Yen H-W, Aikawa Y, Yamamoto S (2014) Change in the chemical composition of infalling gas forming a disk around a protostar. Nature 507(7490):78–80
24. Sakai N, Sakai T, Hirota T, Yamamoto S (2008) Abundant carbon-chain molecules toward the low-mass protostar IRAS 04368+2557 in L1527. ApJ 672(1):371–381
25. Sakai N, Yamamoto S (2013) Warm carbon-chain chemistry. Chem Rev 113(12):8981–9015
26. Sternberg A, Dalgarno A (1995) Chemistry in dense photon-dominated regions. ApJS 99:565
27. Tachihara K, Dobashi K, Mizuno A, Ogawa H, Fukui Y (1996) 13CO (J= 1–0) observations of the lupus molecular clouds. PASJ 48:489–502
28. Tobin JJ, Hartmann L, Chiang HF, Wilner DJ, Looney LW, Loinard L, Calvet N, D'Alessio P (2012) A 0.2-solar-mass protostar with a Keplerian disk in the very young L1527 IRS system. Nature 492(7427):83–85. https://doi.org/10.1007/978-981-19-1708-0_5
29. van der Tak FFS, Black JH, Schöier FL, DJ, van Dishoeck EF (2007) A computer program for fast non-LTE analysis of interstellar line spectra. With diagnostic plots to interpret observed line intensity ratios. A&A 468(2):627–635
30. van Kempen TA, van Dishoeck EF, Hogerheijde MR, Güsten R (2009) Dense and warm molecular gas in the envelopes and outflows of southern low-mass protostars. A&A 508(1):259–274
31. Yıldız UA, Kristensen LE, van Dishoeck EF, Hogerheijde MR, Karska A, Belloche A, Endo A, Frieswijk W, Güsten R, van Kempen TA, Leurini S, Nagy Z, Pérez-Beaupuits JP, Risacher C, van der Marel N, van Weeren RJ, Wyrowski F (2015) APEX-CHAMP$^+$ high-J CO observations of low-mass young stellar objects. IV. Mechanical and radiative feedback. A&A 576:A109
32. Yıldız UA, Kristensen LE, van Dishoeck EF, Belloche A, van Kempen TA, Hogerheijde MR, Güsten R, van der Marel N (2012) APEX-CHAMP$^+$ high-J CO observations of low-mass young stellar objects. III. NGC 1333 IRAS 4A/4B envelope, outflow, and ultraviolet heating. A&A 542:A86